The Astrophysical Journal, 738:168 (14pp), 2011 September 10 doi:10.1088/0004-637X/738/2/168

ENERGY SPECTRUM OF ENERGETIC PARTICLES ACCELERATED BY SHOCK WAVES: FROM FOCUSED TRANSPORT TO DIFFUSIVE ACCELERATION

Pingbing Zuo[1,2], Ming Zhang[1], Konstantin Gamayunov[1], Hamid Rassoul[1], and Xi Luo[1]
[1] Department of Physics and Space Sciences, Florida Institute of Technology, FL 32901, USA
[2] SIGMA Weather Group, State Key Laboratory of Space Weather, Chinese Academy of Sciences, Beijing 100190, China
Received 2011 May 20; accepted 2011 June 17; published 2011 August 23

ABSTRACT

The focused transport equation (FTE) includes all the necessary physics for modeling the shock acceleration of energetic particles with a unified description of first-order Fermi acceleration, shock drift acceleration, and shock surfing acceleration. It can treat the acceleration and transport of particles with an anisotropic distribution. In this study, the energy spectrum of pickup ions accelerated at shocks of various obliquities is investigated based on the FTE. We solve the FTE by using a stochastic approach. The shock acceleration leads to a two-component energy spectrum. The low-energy component of the spectrum is made up of particles that interact with shock one to a few times. For these particles, the pitch angle distribution is highly anisotropic, and the energy spectrum is variable depending on the momentum and pitch angle of injected particles. At high energies, the spectrum approaches a power law consistent with the standard diffusive shock acceleration (DSA) theory. For a parallel shock, the high-energy component of the power-law spectrum, with the spectral index being the same as the prediction of DSA theory, starts just a few times the injection speed. For an oblique or quasi-perpendicular shock, the high-energy component of the spectrum exhibits a double power-law distribution: a harder power-law spectrum followed by another power-law spectrum with a slope the same as the spectral index of DSA. The shock acceleration will eventually go into the DSA regime at higher energies even if the anisotropy is not small. The intensity of the energy spectrum given by the FTE, in the high-energy range where particles get efficient acceleration in the DSA regime, is different from that given by the standard DSA theory for the same injection source. We define the injection efficiency η as the ratio between them. For a parallel shock, the injection efficiency is less than 1, but for an oblique shock or a quasi-perpendicular shock it could be greater.

Key words: acceleration of particles – cosmic rays – shock waves

Online-only material: color figures

1. INTRODUCTION

Collisionless shocks such as planetary bow shocks, traveling shocks driven by coronal mass ejections, the boundaries of corotating interaction regions, and the heliospheric termination shock are frequently observed in the heliosphere. Particle acceleration at shocks has been theoretically and observationally investigated and is believed to directly account for many associated high-energy particle phenomena. Basically, there are three different physical mechanisms involved in the shock acceleration: first-order Fermi acceleration by the converging mirrors in the upstream and downstream regions, shock drift acceleration by the motional electric field at the shock front, and stochastic acceleration (also regarded as second-order Fermi acceleration) if the turbulence is effective. A single encounter with one particle will change a small amount of energy, but due to the scattering by the medium as a diffusion process, both in the upstream and downstream regions, and reflection by the magnetic field kink (in an oblique shock), some particles cross the shock back and forth many times and progressively get to high energy. A family of these diffusion and acceleration processes collectively contribute to the diffusive shock acceleration (DSA) theory, which is currently regarded as a well-established efficient acceleration mechanism applicable to a variety of astrophysical environments (see, e.g., the review by Drury 1983).

Standard DSA theory is conventionally described by the Parker transport equation for the isotropic part of the energetic particle phase space density $f(\mathbf{x}, p)$ (Parker 1965):

$$\frac{\partial f}{\partial t} = \nabla \cdot (\mathbf{K} \cdot \nabla f) - \mathbf{U} \cdot \nabla f - \mathbf{V}_{\rm d} \cdot \nabla f + \frac{1}{3} p \nabla \cdot \mathbf{U} \frac{\partial f}{\partial p} + \frac{1}{p^2} \frac{\partial}{\partial p} \left(D_{pp} p^2 \frac{\partial f}{\partial p} \right), \quad (1)$$

where $\mathbf{K}$ and D_{pp} are the spatial diffusion coefficient tensor and the momentum diffusion coefficient, $\mathbf{U}$ is the speed of background plasma, and $\mathbf{V}_{\rm d}$ is the gradient and curvature drift speed. This equation essentially includes all the major transport effects: convection, drift, spatial diffusion, energy gain or loss by first-order Fermi acceleration and drift acceleration integrated as the acceleration term $dp/dt = -(1/3)p\nabla \cdot \mathbf{U}$ (Jokipii 1982), and second-order Fermi acceleration. The most important success of standard DSA theory is that, from both the macroscopic (solution to the Parker transport equation) and the microscopic (individual particle adiabatic motion) viewpoints, it is able to naturally produce a power-law energy spectrum, and the spectral index depends on the shock strength (compression ratio). The power-law spectrum is a common feature appearing in the observations of all types of energetic particles such as the solar energetic particle (SEP), galactic cosmic ray (GCR), anomalous cosmic ray, etc. Any successful acceleration theory should produce this feature (Giacalone & Kota 2006).

Strictly speaking, in the approximation of diffusion resulting from a strong pitch angle scattering, standard DSA is only

applicable if the pitch angle distribution (PAD) of particles is near-isotropic in the plasma frame. This assumption is not always satisfied, especially for low-energy particles with speeds close to the plasma speed. At the termination shock, the low-energy termination shock particles (TSPs) are observed in the foreshock region with energy below ~20 MeV (Stone et al. 2005). The observations of spacecraft *Voyager 1* and *Voyager 2* indicate that the TSPs are highly anisotropic in the foreshock region even with the beam directly along the heliospheric magnetic field near the termination shock (Decker et al. 2005). Therefore, the acceleration of these particles cannot be described adequately by the standard DSA theory.

In recent years, we have seen dramatic progress regarding the shock acceleration theory. Le Roux et al. (2007) and Florinski et al. (2008a, 2008b) began to apply the focused transport equation (FTE) to study the shock acceleration problem. The FTE describes the evolution of the gyrotropic distribution function $f(\mathbf{x}, v, \mu)$ of energetic particles as the function of space position $\mathbf{x}$, particle speed v, and the pitch angle cosine $\mu = \cos\theta$. It treats the interaction of an energetic particle with the magnetic irregularities as scattering and adiabatic focusing in pitch angle, and the parallel spatial diffusion is replaced by the pitch angle diffusion. The equation is capable of solving the evolution of the particle in μ space with no restriction, allowing the particle distribution function to be highly anisotropic. The applicability of FTE to particle injection at shock waves is rooted in the fact that particles can only move upstream through pitch angle scattering or focusing in combination with the speed of particle streaming. If the speed of a particle is too low or it cannot change in pitch angle, it cannot achieve repeated shock acceleration. This is a fundamental difference from the DSA theory, which relies solely on diffusion (which has an infinite speed on a short timescale) to send particles back upstream. The focused transport theory based on FTE essentially contains all the acceleration processes such as drift, reflection, scattering, etc., which will be discussed in detail in the following sections. Because it is a useful tool for solving the shock acceleration for particle distribution with a large anisotropy, we call it anisotropic shock acceleration theory.

Le Roux et al. (2007) studied pickup ion acceleration in a local area at shocks based on focused transport theory. In their model test, the interstellar core ~1 keV pickup protons are injected and accelerated in the vicinity of a steady-state shock. For the parallel and oblique shocks, the model can roughly produce some of the main features of *Voyager* energetic particle observations near the termination shock, including the intensity spike across the shock, extremely large anisotropy in the upstream, and a power-law energy spectrum at higher energies. At a highly oblique shock, it is found that it is not sufficient to accelerate the original pickup ions because most of the particles encounter the shock only once, and the particles merely get some shock drift acceleration. Florinski et al. (2008a, 2008b) and Florinski (2009) also carried out similar modeling work. A technique of a three-moment expansion using Legendre polynomials to FTE is employed; this is computationally efficient. When the pre-accelerated pickup ions with speed exceeding the injection threshold are injected into the highly oblique termination shock, the shock is able to sufficiently accelerate the pickup ions. Essentially, their simulation can explain the observed anisotropy feature and the intensity spike phenomena near the termination shock. However, a deficiency occurs in this model. Since it only takes limited moments of the FTE expansion in Legendre polynomials, the results are an approximative solution to the full FTE. An important spectral feature obtained in both of the two models is that the acceleration spectrum downstream of the shock at higher energies (compared with the injection particle energy) is a little harder than the prediction of standard DSA theory in the non-parallel shock. Recently, noticing the time-dependent nature of the TSP anisotropy and energy spectrum, le Roux & Webb (2009) adopted a time-dependent focused transport approach by introducing a variable shock obliquity to model the pickup ion acceleration by the termination shock. This simulation successfully reproduces the time variation properties of anisotropy in the pre-shock region of the termination shock observed by the *Voyagers*. In addition, an energy spectrum with multiple power laws is obtained. *Voyager 1* indeed observed the multiple power-law segments separated by spectrum breaks in between as the spacecraft traveled near the termination shock region (Cummings et al. 2006). The successful application of FTE to pickup ion acceleration reveals the promising perspective of the anisotropic shock acceleration theory.

Synthetically, FTE is a five-dimensional parabolic partial differential equation, which is very difficult and time-consuming to solve numerically. Zhang et al. (2009) developed a stochastic approach to solving the FTE via Monte Carlo simulation of stochastic differential equations (SDEs) and applied it to studying SEP transportation in the three-dimensional interplanetary magnetic fields. There is no essential difference between the environment in the vicinity of the shock and the global heliosphere, except that there are discontinuities in the magnetic field and plasma flow for shocks. This approach is computationally very efficient in dealing with a high-dimensional diffusion problem. On this basis, we try to apply this stochastic approach to re-investigate the anisotropic shock acceleration problem in this study. For convenience of comparison with the work of le Roux et al. (2007) and Florinski et al. (2008a, 2008b), we likewise discuss the pickup ion acceleration in the vicinity of the termination shock. The termination shock is modeled as a thin ramp with near-zero thickness, i.e., the discontinuity is treated as a sharp transition region in the magnetic field and plasma background. We also compare the results with the solution of standard DSA theory. Our model can successfully produce the same anisotropy feature and spatial distribution of an energetic particle as that obtained from the models of Florinski et al. and le Roux et al.. We focus our discussion on how the anisotropic shock acceleration theory using FTE is transformed into DSA. Some new intriguing spectral features are revealed. In Section 2, we give the full FTE and discuss its physical content in application to shock acceleration. In Section 3, the general stochastic method for the anisotropic shock acceleration is summarily introduced. We then show the details of the model and the simulation results in the following three sections. The discussion and conclusion are given in the last section.

2. FOCUSED TRANSPORT EQUATION AND ITS APPLICATION TO ANISOTROPIC SHOCK ACCELERATION

FTE has been widely used to model the transportation and acceleration of pickup ions and SEPs in the heliosphere (e.g., Chalov et al. 1997; Klappong et al. 2001; Kota et al. 2005; Zhang et al. 2009). The full FTE for the gyrophase-averaged particle distribution function can be written as (Skilling 1975;

Webb 1985; Isenberg 1997; Zhang 2006; le Roux et al. 2007)

$$\frac{\partial f}{\partial t} = \nabla \cdot \kappa_\perp \cdot \nabla f + \frac{\partial}{\partial \mu} D_{\mu\mu} \frac{\partial f}{\partial \mu} + \frac{1}{p^2} \frac{\partial}{\partial p} \left(D_{pp} p^2 \frac{\partial f}{\partial p} \right) - \frac{d\mathbf{X}}{dt} \cdot \nabla f - \frac{d\mu}{dt} \frac{\partial f}{\partial \mu} - \frac{dp}{dt} \frac{\partial f}{\partial p} + Q_s \quad (2)$$

$$\frac{d\mathbf{X}}{dt} = \mathbf{U} + \mathbf{V}_\mathrm{d} + v\mu\mathbf{b} \quad (3)$$

$$\frac{dp}{dt} = -\left[\frac{1-\mu^2}{2} (\nabla \cdot \mathbf{U} - \mathbf{bb} : \nabla \mathbf{U}) + \mu^2 \mathbf{bb} : \nabla \mathbf{U} \right] p + \mu q \mathbf{E} \cdot \mathbf{b} - \frac{\mu p}{v} (\mathbf{U} \cdot \nabla \mathbf{U}) \cdot \mathbf{b} \quad (4)$$

$$\frac{d\mu}{dt} = -\frac{(1-\mu^2)v}{2L_B} + \frac{\mu(1-\mu^2)}{2} (\nabla \cdot \mathbf{U} - 3\mathbf{bb} : \nabla \mathbf{U}) + \frac{q(1-\mu^2)\mathbf{E} \cdot \mathbf{b}}{p} - \frac{1-\mu^2}{v} (\mathbf{U} \cdot \nabla \mathbf{U}) \cdot \mathbf{b}, \quad (5)$$

where the terms on the right-hand side of Equation (2) are the perpendicular diffusion, pitch angle diffusion, diffusion in momentum space, convection with the solar wind incorporating particle gradient/curvature drift $\mathbf{V}_\mathrm{d}$ (see Northrop 1963 or Rossi & Olbert 1970 for expression), streaming along the magnetic field direction, pitch angle change, and momentum gain or loss, respectively. The terms in the momentum change are the adiabatic cooling or gain, acceleration by the parallel electric field in the plasma frame, and acceleration by inertia force in the plasma frame. The pitch angle change contains the following terms: focusing on the non-uniform magnetic field with a focal length $L_B = (\mathbf{b} \cdot \nabla B)^{-1}$, pitch angle change due to anisotropic adiabatic momentum loss, and pitch angle change due to acceleration by the parallel electric field and by inertia force. It needs to be emphasized that the variables of the momentum and pitch angle are defined in the solar wind plasma frame while the spatial coordinates are defined in a fixed frame. The advantage of the mixed coordinate has been pointed out by Zhang (2006). Equations (2)–(5) are rigorously derived from the quasi-linear theory (e.g., Zhang 2006), except that in those works the last terms in both dp/dt and $d\mu/dt$ were eventually dropped for particles whose speed is much greater than the plasma speed. In this derivation, the only assumption is a quasi-linear approximation with small perturbation amplitude. We believe this equation is valid for all particles in a small perturbation system.

In Equation (2), all the first-order terms come from the adiabatic description of particle motion in an average ambient magnetic field that convects at the speed $\mathbf{U}$. All the formulae are consistent with, e.g., Northrop (1963). Calculation of the parameters for these terms is straightforward once the magnetic field and the plasma velocity field are given. The second-order terms, which we normally call Fokker–Planck diffusion, are from the effect of perturbation due to the presence of electromagnetic fluctuations. For simple cases, the diffusion coefficients can be found in Schlickeiser (2002). Both Zhang (2006) and Schlickeiser (2002) handled more general diffusion that may be necessary for particles in the magnetosphere or interstellar medium. The Fokker–Planck diffusion coefficients $\kappa_\perp$, $D_{\mu\mu}$, and D_{pp} have been studied theoretically by many authors (e.g., Zhang 2006; Schlickeiser 2002; Jokipii 1966). In general, $\kappa_\perp$ depends on the pitch angle cosine. The isotropic form $\mathrm{K}_\perp$ is the average of $\kappa_\perp$ in μ space under the assumption that the isotropic PAD has been used in modeling cosmic-ray modulation and DSA. $D_{\mu\mu}$ is related to parallel diffusion coefficient $\kappa_\parallel$, which is also widely used in modeling cosmic-ray modulation and propagation of SEPs.

Similar to the Parker transport equation, FTE contains all the necessary physics for modeling the shock acceleration of energetic particles, which are included in the acceleration term dp/dt. A portion of shock acceleration comes through the adiabatic energy change term. Although the shock is an abrupt structure, treatment with the adiabatic energy change has yielded surprisingly good results in the diffusive acceleration theory (Drury 1983). This is because the average behavior of particles at a sharp boundary still satisfies the adiabatic approximation (Drury 1983). The pitch-angle-dependent adiabatic energy change formula (Equation (4)) explicitly contains both shock drift acceleration and Fermi acceleration. The drift acceleration is $dp/dt = (1/v)dT/dt = q\mathbf{V}_\mathrm{d} \cdot \mathbf{E}/v$ in the approximation of the static fluid background (Webb et al. 1982), where v is the particle speed and $\mathbf{E}$ is the electric field in a fixed reference frame (Northrop 1963). If we use the frozen-in law $\mathbf{E} + \mathbf{U} \times \mathbf{B} = 0$ and adiabatic gradient-curvature drift approximation (Rossi & Olbert 1970), the perpendicular drift acceleration rate becomes a part of Equation (4), i.e., $(dp/dt)_\perp = -p(1-\mu^2)(\nabla \cdot \mathbf{U} - \mathbf{bb} : \nabla \mathbf{U})/2$, sometimes written as $(dp/dt)_\perp = -p(1-\mu^2)\nabla_\perp \cdot \mathbf{U}_\perp/2$ (Kota 1985). The Fermi acceleration for magnetized particles is due to the speed gradient of scattering medium $(dp/dt)_\parallel = -p\mu^2 \mathbf{bb} : \nabla \mathbf{U}$. In the DSA theory, the shock drift acceleration is implicitly contained in the adiabatic energy change term $-p\nabla \cdot \mathbf{U}/3$ when the particle distribution function is nearly isotropic.

Second, there could be a cross-shock potential that decelerates the solar wind bulk speed and heats up electrons. This potential is important to particle acceleration at low energies. The potential will have a deceleration effect on the particles going through the shock. However, if the cross-shock electric field is large enough in the case of a shock ramp with a thickness close to electron inertia length, the electric field reflects those ions with a small cross-shock speed back to the upstream region. Simultaneous drift along the shock causes the particle to gain momentum through multiple reflections. This process simulates the multiple reflection acceleration or shock surfing suggested by Zank et al. (1996) and Lee et al. (1996). Calculations have been done with an ideal magnetic shock geometry and a very thin shock ramp. A global treatment that incorporates this shock acceleration mechanism could easily be realized using the FTE.

Third, if the speed of the energy particle is comparable to the solar wind speed, as the solar wind slows down abruptly at the shock, the particles feel an inertia force in the solar wind plasma frame (see the term $\mu(\mathbf{U} \cdot \nabla \mathbf{U}) \cdot \mathbf{b}$ in Equation (4)). After subsequent pitch angle scattering and momentum diffusion, the bulk energy is eventually converted to the internal energy of particles.

The FTE can be simplified when applied to the shock acceleration. At the shock, particle acceleration is dominated by the dp/dt term, so we can set the second-order Fermi acceleration coefficient as $D_{pp} = 0$. Moreover, the perpendicular

diffusion is much smaller relative to the parallel diffusion that arises from pitch angle scattering. Only when the shock is almost exactly perpendicular does the perpendicular diffusion become important. Under this condition, the term of perpendicular diffusion can also be omitted. As we know, particle gradient and curvature drift at abrupt boundaries, such as the heliospheric current sheet or the shock, cannot be neglected when we discuss the gyrophase-averaged guiding center drift velocity in the first-order approximation (see le Roux et al. 2007). For shock acceleration, the drift vector of $\mathbf{V}_d$ is always along the shock surface and perpendicular to the gradient of particle intensity. If particle distribution is only a function of the spatial coordinate along the shock normal, the contribution of $\mathbf{V}_d$ to the convection term becomes zero ($\mathbf{V}_d \cdot \nabla f = 0$). The drift velocity $\mathbf{V}_d$ will not directly appear in Equation (3) for a one-dimensional shock geometry. Its effects only show up in the momentum gain as shock drift acceleration.

3. GENERAL STOCHASTIC APPROACH TO SOLVING THE FOCUSED TRANSPORT EQUATION

Zhang (1999, 2000) proposed a stochastic approach with backward SDEs to solving the initial or boundary-value problem of the Fokker–Planck diffusion equation. This method has frequently been applied to the study of modulation of GCR (Zhang 1999; Ball et al. 2005; Luo et al. 2011) and SEP transportation in the heliosphere (Qin et al. 2005; Zhang et al. 2009; He & Qin 2011). Zhang (2000) also summarized how to apply this method to dealing with the shock acceleration from a theoretical perspective. To solve the source injection problem of the Fokker–Planck diffusion equation, it is more convenient to apply the stochastic approach with forward SDEs. Below, we briefly discuss its fundamentals.

The Fokker–Planck equation can be expressed in a general form (Gardiner 1983) as follows:

$$\frac{\partial P(t,\mathbf{q})}{\partial t} = \frac{1}{2}\sum_{\mu,\nu}\frac{\partial^2}{\partial q^\mu q^\nu}G^{\mu\nu}P(t,\mathbf{q}) - \sum_{\mu}\frac{\partial}{\partial q^\mu}K^\mu P(t,\mathbf{q}) + Q(t,\mathbf{q}), \quad (6)$$

where $\mathbf{G}$ is an $n\times n$ diffusion tensor, which is related to an n-dimensional vector $\mathbf{B}$ by

$$\mathbf{G} = \sum_{\mu} B_\mu(t,\mathbf{q})B_\mu^T(t,\mathbf{q}). \quad (7)$$

$\mathbf{K}$ is an n-dimensional vector and the term $Q(t,\mathbf{q})$ represents the injection rate of source particles.

As is well known, this diffusion equation is mathematically equivalent to the system of its forward SDEs:

$$d\mathbf{q} = \mathbf{K}(t,\mathbf{q})dt + \mathbf{B}(t,\mathbf{q})d\mathbf{W}(t), \quad (8)$$

where $\mathbf{W}(t)$ is an n-variable Wiener process. This equation describes the stochastic process of particles in the phase space. Once one particle is injected at $t = t_0$ with the coordinate, $\mathbf{q} = \mathbf{q}_0$ in the phase space. The stochastic trajectory of the particle can be determined by numerically integrating the SDEs. To get the distribution function $f(t,\mathbf{q})$, i.e., the probability density function, a considerable number of test particles are injected in terms of source injection rate $Q(t,\mathbf{q})$, and their stochastic trajectories are simulated. $f(t,\mathbf{q})$ is finally calculated by statistically determining the particle density in the space phase. Due to the equivalence of these two sets of equations, $f(t,\mathbf{q})$ is exactly the solution of the Fokker–Planck equation. As indicated by Krülls & Achterberg (1994), there is no approximation for computing the Fokker–Planck equation using the SDE method. It is one of the advantages compared with other numerical methods.

Now let us return to the FTE. It describes the evolution of distribution function $f(\mathbf{X}, p, \mu)$ in five-dimensional space $(\mathbf{X}, p, \mu)$. It is related to particle energy differential flux or energy spectrum $j(\mathbf{X}, p, \mu)$, which is defined as the number density of particles in phase space element $d\mathbf{X}dpd\mu$:

$$j(\mathbf{X}, p, \mu) = 4\pi p^2 f(\mathbf{X}, p, \mu). \quad (9)$$

The equation governing the evolution of $j(\mathbf{X}, p, \mu)$ can be written in terms of Equations (2)–(5) as

$$\frac{\partial j}{\partial t} = \sum_{i,j}\frac{\partial^2}{\partial x_i \partial x_j}\kappa_{ij}j + \frac{\partial^2}{\partial \mu^2}D_{\mu\mu}j + \frac{\partial^2}{\partial p^2}D_{pp}j - \nabla\cdot\left[\left(\nabla\cdot\kappa_\perp + \frac{d\mathbf{X}}{dt}\right)j\right] - \frac{\partial}{\partial\mu}\left(\frac{\partial D_{\mu\mu}}{\partial\mu} + \frac{d\mu}{dt}\right)j - \frac{\partial}{\partial p}\left[\frac{1}{p^2}\frac{\partial}{\partial p}(p^2 D_{pp}) + \frac{dp}{dt}\right]j + Q_s. \quad (10)$$

Here see Equations (3)–(5) for the expression of $d\mathbf{X}/dt$, dp/dt, and $d\mu/dt$. The conservation equation is a natural consequence of the conservation of the phase space element.

Rewriting Equation (10) to the above standard Fokker–Planck equation form, we get

$$\frac{\partial j(t,\mathbf{q})}{\partial t} = \frac{1}{2}\sum_{\mu,\nu}\frac{\partial^2}{\partial q^\mu q^\nu}G^{\mu\nu}j(t,\mathbf{q}) - \sum_{\mu}\frac{\partial}{\partial q^\mu}K^\mu j(t,\mathbf{q}) + Q(t,\mathbf{q}), \quad (11)$$

with $\mathbf{q} = (\mathbf{X}, p, \mu)$,

$$\mathbf{G} = \begin{pmatrix} 2\kappa_\perp & 0 & 0 \\ 0 & 2D_{pp} & 0 \\ 0 & 0 & 2D_{\mu\mu} \end{pmatrix}, \quad (12)$$

and

$$\mathbf{K} = \begin{pmatrix} \nabla\cdot\kappa_\perp + \dfrac{d\mathbf{X}}{dt} \\ \dfrac{1}{p^2}\dfrac{\partial}{\partial p}(p^2 D_{pp}) + \dfrac{dp}{dt} \\ \dfrac{\partial D_{\mu\mu}}{\partial\mu} + \dfrac{d\mu}{dt} \end{pmatrix}. \quad (13)$$

The corresponding forward SDEs are given by

$$\begin{cases} d\mathbf{X} = \left(\nabla\cdot\kappa_\perp + \dfrac{d\mathbf{X}}{dt}\right)dt + \sqrt{2\kappa_\perp}\cdot d\omega_{\mathbf{X}} \\ dp = \left(\dfrac{1}{p^2}\dfrac{\partial}{\partial p}(p^2 D_{pp}) + \dfrac{dp}{dt}\right)dt + \sqrt{2D_{pp}}d\omega_p \\ d\mu = \left(\dfrac{\partial D_{\mu\mu}}{\partial\mu} + \dfrac{d\mu}{dt}\right)dt + \sqrt{2D_{\mu\mu}}d\omega_\mu. \end{cases} \quad (14)$$

The stochastic approach has many special advantages in application to solving the Fokker–Planck equations numerically. It is more efficient when applied to high-dimensional problems because merely adding a few lines of code is needed to extend one dimension (Zhang 1999). Furthermore, to make a Monte Carlo simulation of SDEs, it is much easier to realize parallel computation even without communication between the computer processors. As will be shown below, the SDE method is especially capable of revealing insights into the physical processes behind the solution to the Fokker–Planck equation since they follow the trajectory and the momentum of individual particles. Owing to such great advantages, the stochastic approach is widely applied to solving the transport problem in cosmic-ray community. This study marks the first time the forward SDE method has been applied to simulate the focused transport process in shock acceleration.

4. MODEL DESCRIPTION

As a first step, we investigate the pickup proton acceleration at the termination shock to reveal the fundamental properties of shock acceleration using the FTE. Pickup ions originate from the ionization of the penetrated interstellar neutral atoms and distribute everywhere from near the sun to the termination shock. As they propagate along with the solar wind to the termination shock, they may undergo second-order Fermi acceleration so that their distribution evolves as the result of diffusion in energy as well as adiabatic cooling. At the termination shock the pickup ions will undergo major acceleration, which will dramatically change their energy spectrum. After the termination shock, the spectrum may continue to evolve due to the second-order Fermi acceleration in the turbulent heliosheath. Here we do not plan to calculate the global accelerated pickup ion distribution spectrum. We merely discuss the acceleration of newly born pickup protons near the termination shock. As we know, these particles tend to form an isotropic spherical distribution in the ambient solar wind frame due to scattering by the ambient Alfvénic waves. Accordingly, mono-energetic (in approximation) protons are continuously and isotropically injected at the vicinity of the termination shock for acceleration. In this study, the acceleration process of such particles by the termination shock is simulated.

For simplicity, we treat the termination shock as a one-dimensional planar shock. We define the X-axis, which denotes the unique spatial coordinates, along the shock normal from downstream to upstream, and the coplanar plane of the plasma flow and magnetic fields as the x–y plane. The plasma flow is normally incident, i.e., in the reverse X-direction ($\mathbf{U} = u\mathbf{e}_x$). Across the shock, the plasma flow is decelerated due to the compression, and the decreased kinetic energy is converted to heat the plasma flow. Here we model compressional flow in the thin ramp transition with a thickness of approximate ion inertia length. The ramp is managed from MHD calculation with balance of momentum flux. The magnetic field profile in the ramp can easily be computed in the tangential electric filed continuity rule ($u_x B_y = \text{constant}$) in accordance with Maxwell equations. The cosine value of the angle between the magnetic field and the shock normal ($\cos\psi = \mathbf{b}\cdot\mathbf{n}$), which determines the direction of the magnetic field in the one-dimensional case, is formulated as

$$\cos\psi = \frac{\cos\theta_{Bn}}{\sqrt{\cos^2\theta_{Bn} + \left(\frac{u_1}{u}\right)^2 \sin^2\theta_{Bn}}}, \tag{15}$$

where θ_{Bn} is the angle between the upstream magnetic field and the shock normal that indicates the shock obliquity, u_1 is the upstream plasma flow speed, and u is the plasma flow speed.

As discussed in Section 2, the stochastic acceleration and the perpendicular diffusion are neglected in the shock acceleration. The drift convection term $\mathbf{V}_d$ is also not considered in the one-dimensional approximation. So the FTE for energy spectrum density is reduced as

$$\frac{\partial j}{\partial t} = \left[\frac{\partial^2}{\partial\mu^2} D_{\mu\mu} - \frac{\partial}{\partial x}(u + v\mu\cos\psi) - \frac{\partial}{\partial p}\left(\frac{dp}{dt}\right) - \frac{\partial}{\partial\mu}\left(\frac{\partial D_{\mu\mu}}{\partial\mu} + \frac{d\mu}{dt}\right)\right] j + Q(x, p, \mu) \tag{16}$$

$$\frac{dp}{dt} = -p\frac{du}{dx}\left(\frac{1-\mu^2}{2}\sin^2\psi + \mu^2\cos^2\psi + \frac{\mu u}{v}\cos\psi\right) + \mu q E\cos\psi \tag{17}$$

$$\frac{d\mu}{dt} = \frac{1-\mu^2}{2}\frac{du}{dx}\left(\frac{v}{u}\sin^2\psi\cos\psi + \mu(1-3\cos^2\psi) - 2\frac{u}{v}\cos\psi\right) + \frac{(1-\mu^2)qE\cos\psi}{p}. \tag{18}$$

This transport equation is a three-dimensional parabolic differential equation (one spatial coordinate for planar shock, momentum, and pitch angle). The corresponding set of forward SDEs is given as

$$\begin{cases} dx = (u + v\mu\cos\psi)dt \\ dp = \dfrac{dp}{dt}dt \\ d\mu = \sqrt{2D_{\mu\mu}}d\omega(t) + \left(\dfrac{\partial D_{\mu\mu}}{\partial\mu} + \dfrac{d\mu}{dt}\right)dt. \end{cases} \tag{19}$$

In Equations (16)–(19), u is the velocity of plasma flow, du/dx is the divergence of the convergent flow, v is the particle speed, and E is the parallel electric field in the plasma frame that may arise from a potential increase. The focused length $L_B = -(\nabla\cdot\mathbf{b})^{-1} = -(u/\sin^2\psi\cos\psi)(du/dx)^{-1}$. Note that the spatial coordinates and the time are measured in the normal incident shock frame, while the momentum, particle speed, and pitch angle are measured in the frame that moves along the plasma flow with non-constant velocity $\mathbf{U}$. The source term in Equation (16) is given by

$$Q(x, p, \mu) = Q_0\delta(p - p_0)\delta(x), \tag{20}$$

where Q_0 is the injection rate of pickup protons convecting into the termination shock. Here we put the termination shock at $X = 0$. The source in Equation (20) means that the particles are injected mono-energetically and isotropically at the shock.

We use the solar wind Parker model for the upstream environment of the termination shock including the magnitude of the magnetic field B_1, the flow speed u_1, and the solar wind number density n_1:

$$\begin{cases} B_1 = B_{\rm E}\left(\dfrac{r_{\rm E}}{r}\right)^2\sqrt{1 + \left(\dfrac{r\sin\theta\Omega_{\rm s}}{u_1}\right)^2} \\ u_1 = u_{\rm E} \\ n_1 = n_{\rm E}\left(\dfrac{r_{\rm E}}{r}\right)^2, \end{cases} \tag{21}$$

where the subscript "E" denotes the values at 1 AU, θ is the polar angle, and Ω_s is the angular speed of the solar rotation. If the compression ratio s and the shock obliquity θ_{Bn} are known, the corresponding downstream parameters can easily be obtained following the standard Rankine–Hugoniot relations

$$\begin{cases} \dfrac{n_2}{n_1} = \dfrac{u_1}{u_2} = s \\ \dfrac{B_2}{B_1} = \sqrt{\cos\theta_{Bn}^2 + s^2 \sin^2\theta_{Bn}}\,. \end{cases} \tag{22}$$

In this simulation, we assume that the termination shock is in the solar equatorial plane $\theta = 90^\circ$ with radial distance $r = 94$ AU so that the normal of the termination shock is in the radial direction. The magnetic field and the plasma parameters at 1 AU are taken as the typical values $B_E = 5$ nT, $u_E = 400$ km s^{-1}, and $n_E = 8$ cm^{-3}. In accordance with the Parker model, the angle between the shock normal and the magnetic field direction θ_{Bn} should be 89.°4. In actual *Voyager 1* observations, the upstream magnetic field near the termination shock varies with the time in a broad range. The average magnetic field direction is nearly perpendicular to the radial direction, as predicted by the Parker model. But in a fraction of time, the angle between the magnetic field and the radial direction is less than 60° and is sometimes even zero. Considering the termination shock configuration change, all kinds of shocks—parallel, oblique, and quasi-perpendicular shocks—may account for the shock acceleration. In this model we do not intend to take into account the role of time variation of the magnetic field in the particle motion. In each simulation, θ_{Bn} is fixed. Different obliquities are designed to study different kinds of shock accelerations (parallel shock, oblique shock, quasi-perpendicular shock, etc.).

For the pitch angle diffusion coefficient $D_{\mu\mu}$ we follow the form that was used in the work of le Roux et al. (2007) and le Roux & Webb (2009). Likewise, we do not aim at a complete self-consistent solution of wave–particle interaction. The expression of $D_{\mu\mu}$ is given as

$$D_{\mu\mu} = D_0 \left[\left(\frac{1}{1+\epsilon} \right) \left(1 - \frac{\mu V_A}{v} \right) \frac{|v\mu - V_A|^{2/3}}{|v\mu - V_A|^{5/3} + (\Omega l_b)^{5/3}} \right] + D_0 \left[\left(\frac{\epsilon}{1+\epsilon} \right) \left(1 + \frac{\mu V_A}{v} \right) \frac{|v\mu + V_A|^{2/3}}{|v\mu + V_A|^{5/3} + (\Omega l_b)^{5/3}} \right] \tag{23}$$

with $D_0 = \pi/8 A^2 \Omega^2 l_b (1-\mu^2)$. Here the parameters V_A, ϵ, Ω, l_b, and A^2 are the Alfvén speed, the relative ratio of backward and forward propagating Alfvén waves, the gyrofrequency of particles, the correlation length, and the wave energy density of magnetic field fluctuation, respectively. For more details, please see the papers of le Roux et al. (2007) and le Roux & Webb (2009).

Our Monte Carlo simulation using the forward SDEs uses the following procedure to calculate the distribution function $f(x, p, \mu) = j(x, p, \mu)/4\pi p^2$. First, the protons are injected at $X = 0$ continuously from $t = 0$ to the time $t = t_{max}$. Since the velocity distribution of the injected particles is considered to be isotropic, the associated pitch angle cosine (μ) is selected as a random number from a uniform distribution in the range of [−1,1]. Then SDEs are solved to get the trajectory of each particle from injection at $t = t_0$ to the ending time $t = t_{max}$. The SDEs are like the first-order ordinary differential equation set that can easily be solved using the Runge–Kutta finite-difference algorithm. The end status (x_e, p_e, μ_e) of each particle is recorded. Additionally, a free escape boundary is set in the upstream and downstream regions. When the particle reaches the free escape boundary, the calculation for the particle motion is ended and the particle is thrown away. We put the escape free boundary several diffusive lengths $l_{diff} = \kappa_{xx}/u$, where $\kappa_{xx} \approx \kappa_\parallel \cos^2\theta_{Bn}$ is the diffusion coefficient. The parallel diffusion coefficient is expressed as

$$\kappa_\parallel = \frac{v^2}{8} \int_{-1}^{1} d\mu \frac{(1-\mu^2)^2}{D_{\mu\mu}}. \tag{24}$$

Finally, the probability of the particle distribution, which is equivalent to the solution of Equations (16)–(18) for the source injection problem, can be constructed by calculating the number density of particles in the phase space cell $\Delta X \Delta p \Delta\mu$.

5. THEORETICAL SOLUTION FOR THE ONE-DIMENSIONAL PARKER TRANSPORT EQUATION AND MODEL TEST

Here we briefly review the solution of the one-dimensional Parker transport equation. In the shock frame, the equation is written as

$$\frac{\partial j}{\partial t} = \frac{\partial}{\partial x}\left(\kappa \frac{\partial}{\partial x} j\right) - \frac{\partial}{\partial x}(Uj) + \frac{\partial}{\partial p}\left(\frac{1}{3}\frac{\partial U}{\partial x} p j\right) + Q(p, x, t). \tag{25}$$

Similarly, the convection drift and the momentum diffusion are not considered here. For a one-dimensional planar shock, all quantities depend spatially on x, and the flow speed is steady and constant except across the shock: $u = u_1$ for $x \leqslant 0$, $u = u_2$ for $x > 0$, and $u_1 > u_2$. The diffusion coefficient is assumed to be independent of the momentum p: $\kappa = \kappa_1$ for $x \leqslant 0$ and $\kappa = \kappa_2$ for $x > 0$. $Q(x, p, t)$ is the source term with the same format as that taken in the anisotropic shock acceleration model: $Q(x, p, t) = Q_0 \delta(p - p_0)\delta(x)$. We select such a simple plasma circumstance because it is then easy to gain the analytical solution for one hand. Most importantly, the solution can basically reveal fundamental features of standard DSA theory such as the acceleration power-law energy spectrum, the intensity distribution in the upstream and downstream regions, etc.

The analytical steady-state solution ($\partial/\partial t = 0$) of Equation (25) for distribution function $f = j/4\pi p^2$ can easily be solved as

$$f = \begin{cases} f_0 p^{-\gamma} e^{-u_1 |x| \kappa_1} & x < 0 \\ f_0 p^{-\gamma} & x \geqslant 0, \end{cases} \tag{26}$$

where

$$f_0 = \frac{\gamma Q_0}{4\pi u_1 p_0^3}. \tag{27}$$

Here, Q_0 is the injection rate, p_0 is the injected energy value, and γ is the spectral index that merely depends on the compression ratio $s = u_1/u_2$ with the expression

$$\gamma = 3s/(s-1). \tag{28}$$

Note that, to get this solution, there is a basic assumption that the particle number density and the number of particles streaming at each momentum are continuous across the shock, which is usually satisfied for isotropic high-energy particles.

The solution indicates that the acceleration energy spectrum inferred from the standard DSA theory is a power-law spectrum

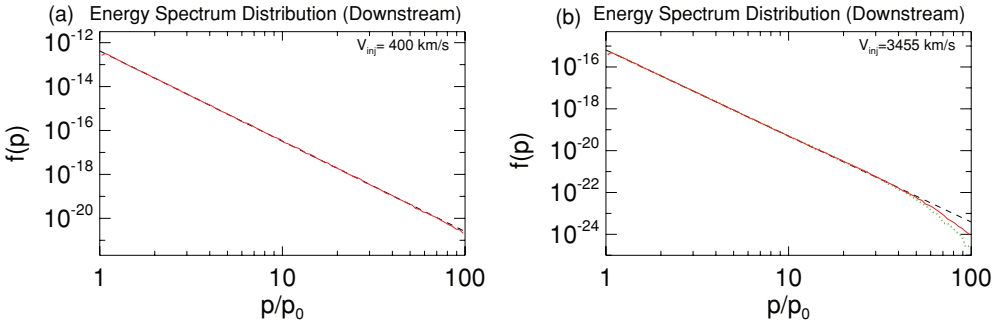

Figure 1. Downstream energy spectrum of energetic particles accelerated by shock in the DSA framework: (a) for the case with the injection particle speed $u_0 = 400$ km s^{-1} and (b) for the case with $u_0 = 3455$ km s^{-1}. The dashed line shows the analytical solution of the Parker transport equation. The solid and dotted lines represent the simulation results using the forward SDE approach.

(A color version of this figure is available in the online journal.)

$f = f_0 p^{-\gamma}$ with the spectral index dependent only on the compression ratio. Another feature is that the intensity increases exponentially in the upstream region and is constant in the downstream. There is no jump across the shock.

As a benchmark test, we apply the forward SDE method to solve the one-dimensional Parker transport equation so as to calculate the energy spectrum distribution in the framework of DSA. The forward SDE sets corresponding to Equation (25) are

$$\begin{cases} dx = \sqrt{2\kappa} d\omega + \left(\dfrac{\partial \kappa}{\partial x} + U \right) dt \\ dp = -\dfrac{1}{3} p \dfrac{\partial U}{\partial x} dt. \end{cases} \quad (29)$$

Two test simulations with different injection particle momentums p_0 are conducted. The shock compression ratio is given as $s = 3.7$ and the upstream solar wind speed as $V_{SW} = 400$ km s^{-1} in both cases. Figure 1 shows the accelerated energy spectrum distribution in the downstream of the shock for the two cases. One is for the injection with a particle speed of $u_0 = 400$ km s^{-1} (see Figure 1(a)), and the other is for $u_0 = 3455$ km s^{-1} (see Figure 1(b)). The black dashed line is plotted in terms of the steady-state analytical solution (Equation (26)). The solid and dotted lines are the numerical simulation based on our model up to time T_{max}. The distribution function $f(p)$ is normalized by setting $Q_0 = 1$. Clearly, as seen in Figure 1(a), there is good agreement between the numerical and analytical results. For the other case presented in Figure 1(b), the simulation results also match well with the analytical solution except that there is a spectrum rollover due to setting the finite acceleration time T_{max} to deal with the time-dependent problem that is usually adopted in the simulation. If we select a larger T_{max}, the start point of the spectral rollover becomes higher, i.e., the rollover shifts to the higher energy. The red solid and green dotted lines present the results for two T_{max} settings. The solid line corresponds to a larger T_{max}. We can see that the start point of the spectral rollover shifts from $p/p_0 \sim 32$ to $p/p_0 \sim 42$. At the momenta below the start point of the spectral rollover, the simulation is well consistent with the analytical solution. To get an accurate solution in the concerned energy range, the appropriate acceleration time T_{max} should be chosen in the simulation. The success of the tests confirms the applicability of the model based on the stochastic approach and proves its accuracy.

6. SIMULATION RESULTS

In this section, we present the simulation results based on our anisotropic shock acceleration model with a focus on the principal features of the accelerated energy spectrum distribution. We discuss three types of shocks with the same shock parameter settings except the shock obliquity θ_{Bn}: parallel shock ($\theta_{Bn} = 0°$), oblique shock ($\theta_{Bn} = 45°$), and quasi-perpendicular shock ($\theta_{Bn} = 80°$). In all the simulations, the shock compression ratio is selected to be $s = 3.7$ and the upstream plasma speed is taken to be $u_1 = 400$ km s^{-1}. The correlation length l_b and wave energy parameter are simply kept constant as $l_b = 0.025$ AU and $A^2 = 0.2$. These parameters are selected to consider a moderate pitch angle scattering near the termination shock. In this paper, the shock-surfing acceleration mechanism due to the effect of cross-shock electrostatic potential is not considered, i.e., we set the parallel electric field to be zero ($E = 0$ in Equations (17) and (18)).

It can be inferred from Equations (17) and (18) that, for energetic particles moving in the steady solar wind environment upstream and downstream of the termination shock, they are only scattered by the magnetic turbulence and waves through the pitch angle diffusion and do not gain or lose any energy adiabatically since there is no convergent flow ($du/dx = 0$) and the momentum diffusion is not considered. Once they cross the shock, however, they experience abrupt changes both in energy and pitch angle due to the drift acceleration, flow compression, adiabatic focusing, pitch angle scattering, etc. When one particle is injected near the shock, it has three possible fates as a first step in the interaction with the shock, depending on its speed and the pitch angle of injection (Decker 1988; Chalov & Fahr 2000): transmitted downstream, reflected to upstream, or moved with no interaction with the shock. Those reflected and non-interaction particles moving upstream from the shock will return to the shock through pitch angle diffusion. Some of them probably can undergo second or multiple encounters with the shock. Similarly, some of the particles in the downstream can also return to the shock for possible energy gain in consecutive shock encounters. In a weak scattering condition, a considerable portion of downstream particles transmitted from upstream cannot change its pitch angle quickly enough to return to the shock, so they simply move downstream and eventually escape. Considering a continuous particle injection, all of these one and multiple shock-crossing particles can be detected and contribute to the energy spectrum distribution.

As far as we know, there have been three numerical models to investigate the pickup ion acceleration in the local area of the termination shock in the framework of anisotropic shock acceleration (also called focused transport acceleration in some literature), namely, the le Roux model (le Roux et al. 2007; le Roux & Webb 2009), the Florinski model (Florinski et al.

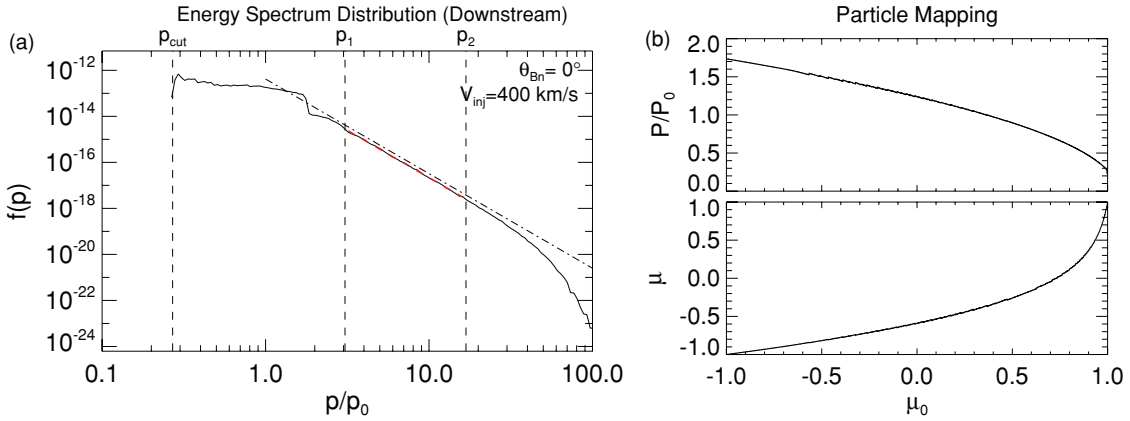

Figure 2. (a) Energy spectrum of energetic particles in the downstream of a parallel shock accelerated in the framework of anisotropic shock acceleration (see the solid line). The red dashed line is the fitted power-law spectrum in the corresponding energy range. For comparison, the analytical solution of the Parker transport equation is also shown (see the dash-dotted line). (b) Particle momentum and pitch angle change vs. the injection particle pitch angle when the particles are injected and interact with the shock transition for the first time.

(A color version of this figure is available in the online journal.)

2008a, 2008b; Florinski 2009), and the Chalov model (Chalov & Fahr 2000). In Chalov's model, the pickup ion's trajectory in the upstream or in the downstream is calculated by the SDEs corresponding to FTE, and when the particles interact with a shock, the energy and pitch angle changes are determined in terms of adiabatic test particle theory (Webb et al. 1983). Although the stochastic method is applied, the Chalov model is much different from our current model, in which the acceleration process in the shock ramp is also directly governed by the stochastic different equations. All three models are able to calculate the accelerated energy spectrum that is proved to have two components: one is the low-energy component, which is due to the first transmitted particles and/or the two shock-encounter particles, and the other is the high-energy component, which is due to the multiple shock-encounter particles (Chalov & Fahr 2000, le Roux et al. 2007). Below we present our modeling results regarding the acceleration energy spectra. Comparison with previous studies is also discussed.

6.1. Parallel Shock

Figure 2(a) shows the accelerated energy spectrum distribution downstream of a parallel shock ($\theta_{Bn} = 0^\circ$). The dash-dotted line is the analytical solution of the one-dimensional Parker transport equation (Equation (26)), and the solid line is our simulation result using FTE. The distribution function is normalized by setting $Q_0 = 1$ (similarly hereinafter). Here we inject particles continuously and isotropically upstream of the shock, with the particle speed the same as the upstream solar wind speed, i.e., $v_{\rm inj} = u_1 = 400$ km s^{-1}. The spectrum can be roughly divided into two parts, excepting a spectrum rollover at high energies that is caused by limited acceleration time as indicated in the model test in Section 5. Between $0.27 < p/p_0 < 3.1$, the spectrum is complicated but contains most of the injected particles. At the higher energy part between $3.1 \leqslant p/p_0 \leqslant 16.8$, it is characterized by a power-law distribution (see the region bounded by two vertical lines labeled by p_1 and p_2, respectively). Figure 2(b) presents the particle momentum and pitch angle change versus the injection particle pitch angle when the particles are injected and interact with the shock transition for the first time based on the FTE. In our model, the magnetic field is set in the upstream direction, so a particle with $\mu_0 = -1$ means that it moves along the shock normal to downstream. For a parallel shock, the magnetic field is constant across the shock ramp, so the particles injected with a speed equal to the upstream solar wind speed will not be reflected, that is, transmitted downstream. It can be seen from Figure 2(b) that the downstream pitch angle μ and the momentum p change smoothly with the injection pitch angle μ_0. Within one interaction with the shock, those injected particles with $\mu_0 > 0$ suffer energy loss with a maximum loss to $p_{\rm min} = 0.27\,p_0$. Those with $\mu_0 < 0$ gain energy with a maximum boosting to $p_{\rm max} = 1.7\,p_0$. The momentum of the transmitted particles in the downstream after crossing a parallel shock can also be estimated by the equation analyzed in the paper of le Roux et al. (2007):

$$p/p_0 = \sqrt{1 + \left(\frac{s}{s+1}\right)^2 + 2\mu_0 \left(\frac{s}{s+1}\right)}. \qquad (30)$$

The energy range of the transmitted particles estimated by the above equation is [0.27 p_0~1.7 p_0]. In this energy range, the spectrum is roughly a hard power-law distribution that ends at a momentum of $p = 1.7\,p_0$. This part of the spectrum is made up by the initially transmitted particles. The lower energy cut-off momentum is right at the minimum momentum of the transmitted particles (see the vertical line labeled as "$p_{\rm cut}$"). There is a sharp decrease at $p = 1.7\,p_0$ followed by a small bump in a narrow energy band until $p = 3.1\,p_0$. This part of the spectrum is made up by those scattered by the downstream turbulence back to encounter the shock another time. As analyzed by le Roux et al. (2007), the decrease and the bump in the narrow energy range are formed due to these particles. Some of the transmitted particles are eventually able to cross the shock multiple times. These particles contribute to a power-law distribution spectrum between $3.1 < p/p_0 < 16.8$. The line fitting to the spectrum in this range (the red dashed line) is parallel to the DSA spectrum line (the dash-dotted line). The slope of the fitting spectrum calculated is $\gamma_{\rm fit} = 4.11 \pm 0.01$, which is the same as the theoretical prediction of standard DSA, i.e., $\gamma_{\rm DSA} = 3s/(s+1) = 4.11$ for a compression ratio $s = 3.7$. This is consistent with the result for parallel shock acceleration in le Roux et al. (2007), in which they pointed out that, as long as particles can have multiple shock encounters, the DSA theory still holds even if the anisotropy is not small.

Usually, the acceleration efficiency by the shock is represented by the flux of accelerated energy particles at certain

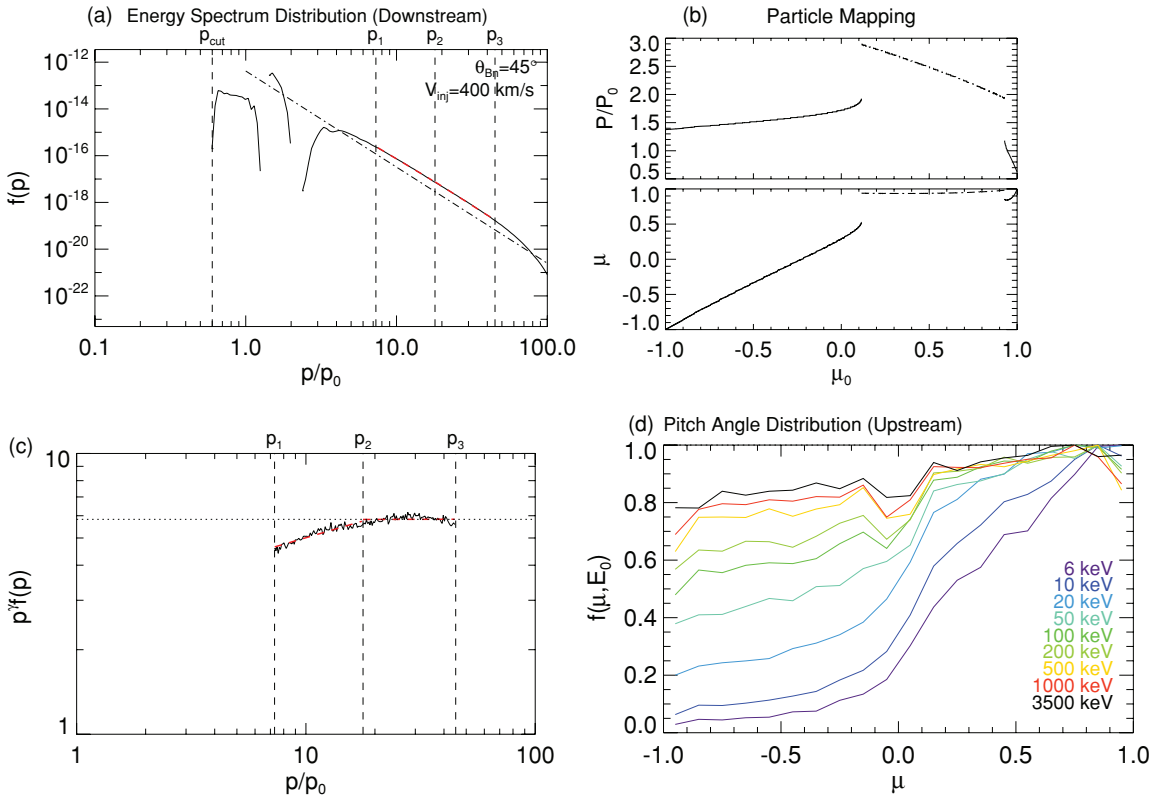

Figure 3. (a) Energy spectrum of energetic particles downstream of the oblique shock with obliquity $\theta_{Bn} = 45^\circ$ accelerated in the framework of anisotropic shock acceleration with the same format as that in Figure 2(a). (b) Particle momentum and pitch angle change vs. the injection particle pitch angle when the particles are injected and interact with the shock transition for the first time. The solid line shows the particles transmitted downstream and the dash-dotted line is for the particles reflected by shock. (c) Distribution function $p^\gamma f(p)$ with high resolution in the energy range where the accelerated energy spectrum is a double power-law spectrum. (d) Upstream pitch angle distributions $f(\mu)$ of the energetic particles at certain energies. $f(\mu)$ is normalized by its maximum.

(A color version of this figure is available in the online journal.)

momentum $j(p) = 4\pi p^2 f(p)$ relative to the number density $n = \int_0^\infty j(p)dp$, that is, $j(p)/n$. As seen in Figure 2(a), the simulated intensity of the power-law distribution at higher energies is smaller compared with the solution of standard DSA theory. That means less particles are able to accelerate to high energy. We can therefore conclude that, for a parallel shock, the efficiency to accelerate to the standard DSA regime at higher energies is less than 1. Here we define the injection efficiency η as the ratio of the acceleration particle flux at the power-law energies obtained by the anisotropic shock acceleration to the flux from the DSA. Since the power-law slope is the same, η should be equal to the ratio of energy spectrum intensity, i.e., $\eta = f(p)/f_{\rm DSA}(p)$. At this parallel shock, for injected pickup ions with a speed equal to the solar wind speed, the injection efficiency is calculated as $\eta = 0.67$.

6.2. Oblique Shock

Figure 3(a) presents the downstream accelerated energy spectrum for an oblique shock with obliquity $\theta_{Bn} = 45^\circ$, as well as the momentum of the injection pickup ions $p_0 = mu_1$. At the energies $p/p_0 < 7.3$, the energy spectrum is more complicated. In this range the spectrum appears to be broken into several pieces separated by empty gaps. At momentum $p < p_0$ corresponding to particle energy loss, similar to that in the parallel shock, the spectrum first increases and then resembles a hard power-law distribution, and there is low-energy cutoff at $p \sim 0.6\, p_0$. Following this, there are two spectral gaps and two peak structures in the spectrum at momenta $p > p_0$. The distribution gap means no particles fall into this energy range. It can be proved that the spectrum at the energies below $p \leqslant 1.9 p_0$ is formed by particles that interacted with the shock once. Across a fast oblique shock, the magnetic field is kinked, with the field direction changed and the magnitude enhanced. One particle across the shock undergoes gradient drift and curvature drift, which results in the particle energy gain or loss by the motional electric field. Figure 3(b) records the momentum and pitch angle change when the particles interact with the shock ramp for the first time after injection. After the new-born pickup ions with a speed equal to the upstream solar wind have been injected, some of them are transmitted through the shock ramp downstream, and the rest are reflected to return upstream due to the magnetic field kink that makes the acceleration process different from that in the parallel shock. The mappings of pitch angle and momentum for these two kinds of particles are, respectively, shown as the solid line and the dash-dotted line in Figure 3(b). The particles with pitch angle $0.12 < \mu_0 < 0.93$ are reflected with an enhanced momentum. The gained momentum is distributed between $p_{\rm min} = 1.9\, p_0$ and $p_{\rm max} = 2.9\, p_0$. Note that, after particles are reflected, the particle pitch angle is roughly along the magnetic field in the upstream direction ($\mu = 0.93 \sim 0.98$), which will directly result in a highly anisotropic beam in the upstream region. Some of the particles transmitted downstream through the shock ramp lose energy in the downstream solar wind frame with a minimum momentum $0.6\, p_0$, and a significant portion of the transmitted particles gain energy with the maximum momentum $1.9\, p_0$. As a whole, the energy gain of the transmitted particles is less

Table 1
The Fitted First-order and Second-order Anisotropy of Energetic Particles in the Upstream of the Shock at Nine Energies

E	6 keV	10 keV	20 keV	50 keV	100 keV	200 keV	500 keV	1000 keV	3500 keV
p/p_0	2.6	3.4	4.8	7.6	10.8	15.2	24.1	34.1	63.8
ξ_1	1.48	1.25	0.88	0.55	0.37	0.29	0.18	0.14	0.12
ξ_2	0.50	0.25	0.06	0.001	−0.01	−0.01	−0.02	−0.01	0.0004

than that of the reflected particles, which is consistent with the shock-drift theory (Webb et al. 1983). The energy range of the particles interacting with the shock for the first time (reflected or transmitted) is [0.6–1.02] ∪ [1.39–1.9] p_0. No particle falls into the narrow energy range [1.02–1.39] p_0. This corresponds to the first distribution gap. Additionally, the low-energy cutoff is $p_{\rm cut} = 0.6p_0$, that is, right at the minimum momentum of the particles transmitted downstream for the first time. After the first interaction with the shock ramp, a portion of the reflected particles will be scattered back by turbulence. They return to the shock and undergo another energy gain or loss. The energy differences between the first and second shock interactions form a second spectral gap between $2.1 < p/p_0 < 2.4$.

We wish to emphasize the energy spectrum at high energies. Similar to the parallel shock, the spectrum at the high energies is contributed by the particles having gone through multiple shock encounters. As shown in Figure 3(a), the spectrum can be approximated by a double power-law spectrum at the momenta between $p_1 = 7.3p_0 < p < p_3 = 46p_0$ (see the region bounded by two vertical lines labeled as "p_1" and "p_3"). For comparison, the analytical solution of DSA from the one-dimensional Parker equation is also plotted as a dash-dotted line. To show this double power-law spectrum more clearly, we plot the distribution function $p^\gamma f(p)$ in the energy range $p_1 < p < p_3$ in Figure 3(c) separately. Here, γ is the spectral index of the standard DSA with value $\gamma = 3s/(s-1) = 4.11$ for a compression ratio $s = 3.7$. It can be seen that the first power-law spectrum between p_1 and $p_2 = 17.7p_0$ is a little harder than the standard DSA spectrum. The corresponding fitting slope of the spectrum is $\gamma_1 = 3.87 \pm 0.01$. This result is in agreement with the work of le Roux et al. (2007), where it is also a harder power-law spectrum for $6 < v/u_1 < 10$ with fitting index $\gamma \sim 3.9$ for oblique shock acceleration (the same given compression ratio). Their simulation, however, did not give the real spectrum at higher energies due to a low spectral rollover. Here we extend the calculation to the higher energy until $p = p_3 = 46p_0$ where the spectral rollover starts. The fitting line between p_2 and p_3 with the second power-law spectrum is exactly parallel to the dash-dotted line. The slope difference between the two fitting power-law spectra is much more evident in Figure 3(c). The corresponding fitted spectral index for the second power law is $\gamma_2 = 4.11 \pm 0.01$. It implies that, in this energy range, the particles have gone into the DSA regime. It can be seen that the double power-law spectrum line is far above the spectrum line given by standard diffusive acceleration theory. It indicated that more particles can cross the shock multiple times so that they are accelerated to high energies. The acceleration efficiency is improved. In the energy interval $p_2 < p < p_3$, the injection efficiency η defined above is 2.57, which far exceeds 1.

From the microscopic viewpoint of the diffusion acceleration theory, the average momentum change of particles for each shock crossing plays a decisive role in determining the spectrum slope at certain momentum, which depends on the particle acceleration rate, i.e., $\langle 1/pdp/dt\rangle$ averaged over all pitch angles (see the review of Drury 1983). For an isotropic PAD, $\langle 1/pdp/dt\rangle = -(1/3)du/dx$, which is independent of the particle momentum so that the power-law distribution with spectral index $\gamma = 3s/(s-1)$ is generated. Now we consider the case in which the pitch angle distribution $f(\mu)$ is anisotropic at any momentum p. For simplicity of discussion, let us expand it as a sum of Legendre polynomials to the second order:

$$f(\mu) = \xi_0[P_0(\mu) + \xi_1 P_1(\mu) + \xi_2 P_2(\mu)], \tag{31}$$

where $P_i(\mu)$ is the i-order Legendre polynomial and ξ_i is defined as the i-order anisotropy coefficient ($i = 0, 1, 2$). So the average particle acceleration rate in the shock ramp can be derived as

$$\left\langle \frac{1}{p}\frac{dp}{dt}\right\rangle = \frac{\int_{-1}^{1} f(\mu)\frac{1}{p}\frac{dp}{dt}\,d\mu}{\int_{-1}^{1} f(\mu)\,d\mu} = -\frac{1}{3}\frac{du}{dx}\left[1 + \frac{u}{v}\cos\psi\xi_1 + (0.6\cos^2\psi - 0.2)\xi_2\right]. \tag{32}$$

Here the original acceleration rate is given by Equation (17). At high energies where particle velocity is much greater than the solar wind speed, i.e., $v/u \gg 1$, the effect of the first-order anisotropy ξ_1 can be reasonably neglected so that the average acceleration rate only depends on the second-order anisotropy ξ_2. For the high-energy particles, the second-order anisotropy becomes important to the determination of the spectrum slope. When ξ_2 is small in a high-energy range, the average acceleration rate is reduced to the same form as that from the isotropic condition, so that a power-law spectral index in this energy range only depends on the compression ratio. In this sense, the particle acceleration has gone into the standard DSA regime, although the particles are not isotropic.

To calculate the PAD at certain momentum so as to determine the anisotropy coefficients, one should record the pitch angle information for all of the particles that are able to accelerate to reach this momentum at the arrival time in the shock transition where the particle energy changes take place. According to the simulation results of le Roux et al. (2007) and Florinski et al. (2008a, 2008b), the particles are isotropic in the downstream, and mostly anisotropic in the upstream. There are few particles in the upstream region at any time, so to estimate the anisotropy at certain momentum, we approximate the PAD at some energies by statistically counting all the particles in the upstream region and expanding the PAD in Legendre polynomials. This allows us to roughly estimate the anisotropy feature. Figure 3(d) gives the PAD of all upstream particles at nine energy points. The corresponding first- and second-order anisotropy coefficients are listed in Table 1. It is evident that the upstream particles are strongly anisotropic, even at the energy of ∼1 MeV. The first-order, and most dominant anisotropy, decreases with the increasing energy. This feature is also obtained in the work of le Roux et al. (2007). As discussed above, the particles reflected

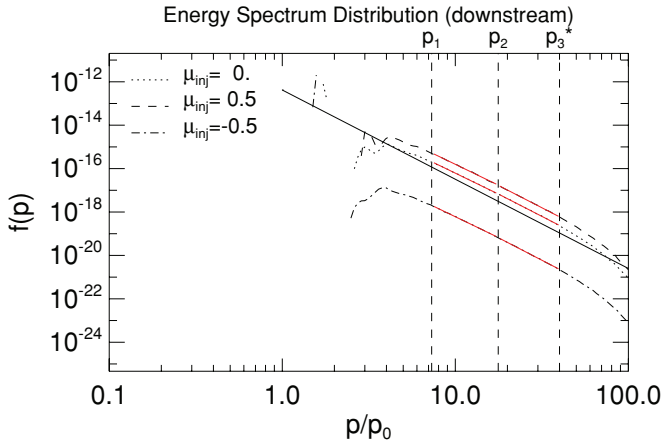

Figure 4. Downstream energy spectrum of energetic particles accelerated by shock with obliquity $\theta_{Bn} = 45^\circ$ for three cases where the seed pickup ions are injected with pitch angles $\mu_{\rm inj} = 0$, 0.5, and -0.5, respectively.

(A color version of this figure is available in the online journal.)

upstream by the shock for the first time form a beam almost along the magnetic field in the upstream region (see Figure 3(b)), so it is the most anisotropic in the energy range of reflected particles ($1.9 < p/p_0 < 2.9$). For the particles experiencing multiple shock crossings, although the first-order anisotropy is still not small, the second-order anisotropy decreases much more rapidly (less than 0.05, see the ξ_2 at $E \geqslant 50$ KeV). At $E = 3.5$ MeV, the second-order anisotropy is very close to zero. We note that the above anisotropy analysis is an approximation since in the entire upstream the statistics is very poor. Nevertheless, it qualitatively gives the anisotropy change with the particle energy. At the energies of the power-law spectrum, the second anisotropy is evidently small enough, although the first anisotropy is still large. The formation of the double power-law distribution can be explained based on the second-order anisotropy. At higher energies corresponding to the second power-law spectrum, because the second anisotropy is nearly zero, the spectral index is not different from that of the standard diffusive acceleration. Note that the particle speed is already far larger than the solar wind speed. At lower energies corresponding to the first power-law spectrum, because the second-order anisotropy is small but not zero and keeps roughly constant, the spectrum slope at each momentum in this energy range is slightly smaller than the predicted spectral index of standard DSA. Therefore, the spectrum line can be fitted with a harder power-law distribution spectrum.

After the seed particles have been injected upstream of the shock, they are selectively reflected or transmitted downstream according to their pitch angle. This results in an anisotropic distribution for these first shock encounter particles. When they continue to cross the shock back and forth consecutively, however, motion in the upstream and downstream makes the particles more and more isotropic by pitch angle scattering (see the pitch angle diffusion term in Equation (18)). Eventually, at certain higher energy, the second-order anisotropy becomes very small, so that the DSA mechanism plays the major role. This process is developed whether the seed particle is isotropic or anisotropic. To verify this point, we conduct test simulations by injecting the new-born pickup ions with mono-pitch-angle rather than isotropically. Figure 4 presents the downstream energy spectrum distribution for three cases with the injection pitch angles of 0, 0.5, and -0.5, which are shown in the dotted line, the dashed line, and the dash-dotted line, respectively. The solid line is plotted in terms of standard DSA theory. It is clearly seen that in the momentum between $p = p_1$ and $p = p_3^* = 40p_0$, the spectra are similar to a double power-law spectrum with the joint at $p = p_2$ for each case. Here p_3^*, not p_3, is selected because at the momentum p_3^*, the spectrum starts to roll over for the case $\mu_0 = 0.5$. The segmental fitting indexes for the three spectra are listed in Table 2. The fitting indexes for the three cases are in agreement with the case with isotropic injection discussed above. This indicates that the particle anisotropy at a certain momentum larger than p_1 is independent of the pitch angle of the initial injection particles. The main difference between the three spectra at high energies is that the injection efficiency is not the same. The acceleration efficiency is relevant to the probability of returning to the shock for multiple encounters, which is seriously dependent on the particle pitch angle in the given scattering circumstance. With a different injection particle pitch angle, the proportion of the particles able to gain multiple shock crossing is different, resulting in the different injection efficiency. A big difference can be seen in the low-energy part of the energy spectrum for the three cases and the case with isotropic injection. This is easy to understand since this part is contributed by the particles transmitted through or reflected by the shock for the first time. For these particles, the energy gain or loss is sensitive to the injection particle pitch angle (see the mapping plot). Their intensity and energy distribution range also depend on the initial injection momentum and the pitch angle. If we inject the particles with pitch angle $\mu_0 = 1$, all of the particles are just transmitted downstream with energy loss (see the mapping plot in Figure 3(b)), and they cannot return to the shock for another shock encounter due to the low speed. In addition, our spectra at the low-energy part are very different from those given by le Roux et al.'s simulation for both the parallel shock and the oblique shock (see Figures 1(a) and 6(a), respectively, in le Roux et al. 2007). This is due to the different injection spectrum. In le Roux et al.'s (2007) simulation, they injected particles in the whole upstream region. When particles move from the injection location to the termination shock, their momenta are expected to decrease due to adiabatic cooling in their model, so the seed particles injected for shock acceleration are no longer mono-energetic, but include a considerable number of particles with speeds lower than the upstream solar wind speed. That is why we cannot see a low-energy cutoff above $p/p_0 = 0.1$ in their simulation.

Table 2
The Fitted Spectral Indexes of the Double Power-Law Spectrum

Injection	γ_1 ($p_1 \sim p_2$)	γ_2 ($p_2 \sim p_3^*$)
$\mu_0 = 0$	3.87 ± 0.02	4.09 ± 0.02
$\mu_0 = 0.5$	3.86 ± 0.03	4.10 ± 0.03
$\mu_0 = -0.5$	3.85 ± 0.02	4.12 ± 0.02
Isotropic injection	3.87 ± 0.01	4.11 ± 0.01

Notes. γ_1 is fitted between $p_1 < p < p_2$ and γ_2 is fitted between $p_2 < p < p_3^*$. See the text for the values of p_1, p_2, and p_3^*.

6.3. Quasi-Perpendicular Shock

We now consider the anisotropic acceleration by a quasi-perpendicular shock with an obliquity of $\theta_{Bn} = 80^\circ$. For a highly oblique shock, once transmitted upstream to downstream, the particles cannot easily return to the shock since the magnetic

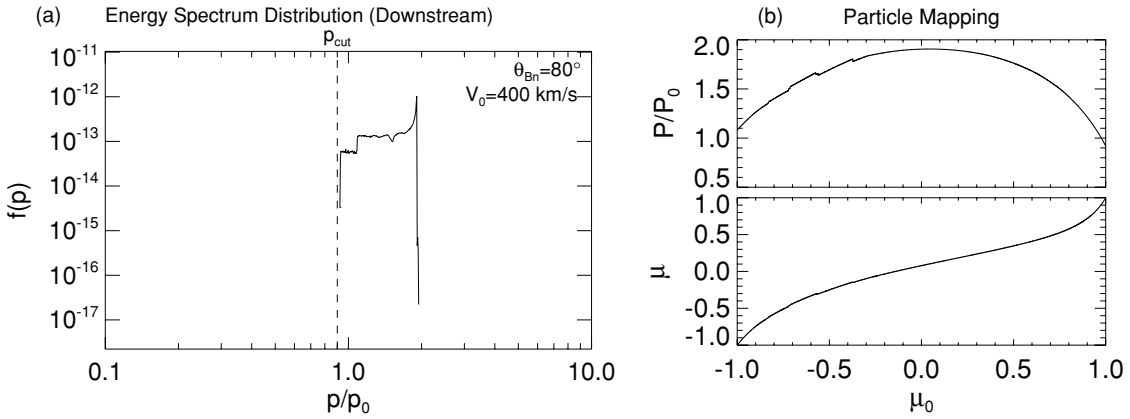

Figure 5. (a) Energy spectrum of energetic particles in the downstream of the oblique shock with obliquity $\theta_{Bn} = 80^\circ$ accelerated in the framework of anisotropic shock acceleration. (b) Particle momentum and pitch angle change vs. the injection particle pitch angle when the particles are injected and interact with the shock transition for the first time. The injection particles' speed is 400 km s^{-1}.

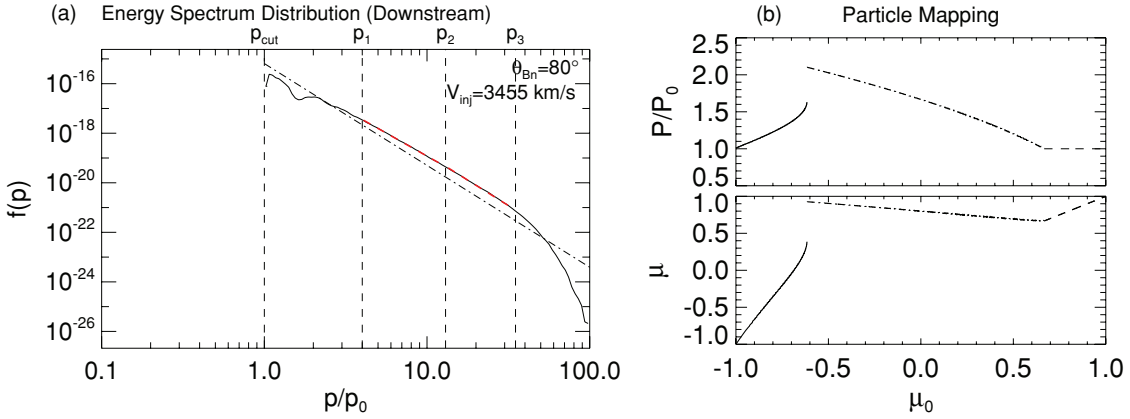

Figure 6. Same as Figure 5 except that the injection particles' speed is 3455 km s^{-1}.
(A color version of this figure is available in the online journal.)

field is nearly perpendicular to the shock normal. To return upstream, the particle speed needs to meet $v > u_2/\cos\theta_2 \simeq u_1/\cos\theta_{Bn}$, where u_2 and θ_2 are the downstream solar wind speed and the particle pitch angle, respectively (Decker 1988). For a shock with $\theta_{Bn} = 80^\circ$, the speed threshold is roughly six times the upstream solar wind speed, that is, much larger than that for the oblique shock and the parallel shock. Here we discuss two cases: injection of the newly born pickup ions with $v_0 = u_1$, and injection of pre-accelerated particles with $v_0 = 1.5u_1/\cos\theta_{Bn}$. Similarly, the source particles are injected continuously and isotropically near the shock.

Figure 5 gives the downstream energy spectrum and the particle mapping for the first case, with the same format as Figure 2. It can be seen that all the injected particles are transmitted downstream without any reflection as seen in the situation in the parallel shock. The particle momentum changes smoothly in the range between $0.9 < p/p_0 < 1.9$ along with the initial injection pitch angle. The maximum speed of the particles after being transmitted is about $1.9u_1$, which is much smaller than the threshold $u_1/\cos\theta_{Bn}$. All the particles cannot return to the shock, i.e., simply escape along with the solar wind and no particle experiences multiple shock encounters. These particles make up the energy spectrum in a narrow energy range with low-energy cutoff $p_{\rm cut} = 0.9p_0$ and high-energy cutoff $p'_{\rm cut} = 1.9p_0$, which are equal to the minimum and the maximum momentum of the transmitted particles, respectively.

In Figure 6, the downstream energy spectrum and the particle mapping are shown for the case of $v_0 = 1.5u_1/\cos\theta_{Bn} =$ 3455 km s^{-1}. The particles undergo three kinds of tracks after injection depending on their pitch angles: transmitted downstream, reflected, or non-interacting with shock. The momentum and pitch angle changes are denoted for these three kinds of particles as solid, dash-dotted, and dashed lines, respectively, in Figure 6(b). Both the transmitted and the reflected particles are accelerated. The non-interaction particles and reflected particles will change pitch angle due to the scattering when moving in the upstream, and some could return to the shock for further acceleration. It can be seen that the pitch angle of the reflected particles distributes in a narrow range (0.66–0.93), similar to the situation in the oblique shock, which is expected to lead to strong anisotropy at corresponding energies. A portion of transmitted particles will then return to the shock since their energy is above the speed threshold for returning, so that they can undergo similar processes taking place in the oblique shock and the parallel shock: scattering by the upstream and downstream scattering center, crossing the shock back and forth. Eventually in the upstream and downstream region, particles of various energies can be found. Let us return to the energy spectrum shown in Figure 6(a). It can be seen that in the lower energy part (relative to the injection particle energy), there are two peaks with a spectrum dip between. The spectra dip is also produced in both Florinski's model and Chalov's model (Florinski et al. 2008b;

Chalov & Fahr 2000), which is a consequence of efficient acceleration by adiabatic reflection. This low-energy part of the spectrum is generated by particles that encountered the shock once or twice. At the higher energy part, there is a power-law distribution contributed by the multiple shock-encounter particles, similar to the oblique shock. Between $4.0 < p/p_0 < 13$ corresponding to the first power-law spectrum, the fitting spectral index is 3.71 ± 0.01, i.e., it is harder than the standard diffusive acceleration spectrum. Between $13 < p/p_0 < 35$ corresponding to the second power-law spectrum, the fitting spectral index is 4.11 ± 0.03. This indicates that in this energy range, the particle acceleration has fallen into the DSA regime. Similar to the oblique shock, the injection efficiency is above 1 with $\eta = 2.71$.

From the above analysis, it can be concluded that the highly oblique shock is not sufficient to efficiently accelerate the low-energy particles like the newly born pickup ions. Le Roux & Webb (2009) pointed out that the injection threshold of DSA in focused transport is given by $v_0 > u_1/\cos\theta_{Bn} = v_{\rm dHT}$, where $v_{\rm dHT}$ is the de Hoffmann–Teller speed. The accelerated energy spectrum at the momenta over multiple times injection momentum is a double power-law distribution. In addition, the reflection causes large anisotropy at the momenta around the injection particle momentum.

7. DISCUSSION AND CONCLUSION

In previous studies, the focused transport theory has been proved by *Voyager 1* and *Voyager 2* to be an efficient tool for reproducing the observational features of the lower energy TSPs, such as the anisotropy distribution, intensity spike, multiple power-law energy spectrum, and so on (le Roux et al. 2007; le Roux & Webb 2009; Florinski et al. 2008a, 2008b; Florinski 2009). This is difficult to explain with the standard DSA theory. Here we investigate the pickup ion acceleration at three kinds of shocks with varying obliquity in the framework of focused transport theory. Our focus is on the accelerated energy spectra and their transition from anisotropic acceleration to DSA. Some intriguing new knowledge about the anisotropic shock acceleration is obtained. First, we confirm that the shock acceleration leads to the two-component spectral distribution. From the particle pitch angle and momentum mapping across the shock, the shape of the low-energy component of the spectrum is contributed by the particles interacting with the shock once or a few times. The spectral shape sensitively depends on the momentum and pitch angle of the injection particles. For a parallel shock, the high-energy component of the spectrum is a power-law spectrum with a spectral index equal to the prediction of the standard DSA theory. For an oblique or quasi-perpendicular shock, if the particles can be accelerated to cross the shock back and forth for multiple times, the high-energy component of the spectrum is formed and is represented as a double power-law distribution: a harder spectrum with slope less than the spectral index of the standard DSA spectrum followed by another power-law spectrum consistent with the DSA at higher energies.

We found that the spectrum slope at high energies depends on the second-order anisotropy. The formation of the double power-law distribution can be explained according to the anisotropy distribution under the combination of adiabatic focusing by shock and the pitch angle scattering in upstream and downstream media. The anisotropic shock acceleration will eventually go into the DSA regime at higher energy, where the second-order anisotropy is close to zero, although the first-order anisotropy can still be large.

We compare the intensity of the energy spectrum given by the anisotropic shock acceleration with that given by the DSA for the same injection and find that the acceleration efficiency is different even at high energies. To measure the acceleration efficiency, we define the injection efficiency as the ratio of the intensity of the distribution functions given by the two acceleration theories in the high-energy range where particles get into the standard DSA regime. The DSA takes a built-in assumption that particles are accelerated entirely according to the probability of shock crossing. For a parallel shock, a considerable number of particles are decelerated. They cannot return to the upstream so the probability of getting multiple shock crossings is low. The injection efficiency is reduced below 1. For the oblique shock or quasi-perpendicular shock, the reflection due to the magnetic field kink makes particles cross the shock and gain energy, resulting in improved acceleration efficiency. The injection efficiency could be significantly larger than 1.

The observations of the energetic ions by the two *Voyager* spacecraft in the vicinity of the termination shock provide us with essential information about pickup ion acceleration. Cummings et al. (2006) found that the energetic proton tends to form a spectrum of exceptional four power laws that may be evidence of two-component acceleration: at low energies the energy spectrum is a double power-law spectrum with a break at 0.4 MeV; a second component appears above 1 MeV, consisting of two power-law spectra with a break at 3.2 MeV. Le Roux & Webb (2009) developed a time-dependent model in which the time variation in the magnetic field angle from the average angle is taken into account. This model successfully produces multiple power-law energy spectra with steady break points in the upstream spectrum. According to the current understanding of anisotropic shock acceleration, we can give some supplementary reasons why the multiple power-law spectra are naturally produced in the observations and in the modeling. As we know, the termination shock has an obliquity of $\sim 90^\circ$ on average. The analysis in the above section tells us that for such a highly oblique shock, the newly born pickup ions with speed nearly equal to the solar wind speed are not able to accelerate and are simply transmitted to the heliosheath. However, the magnetic field observation of *Voyager 1* near the termination shock indicated that the resulting shock obliquity deviates from the average angle of 90° to less than 60°, i.e., this shock is no longer a quasi-perpendicular shock in a significant fraction of time. During the magnetic field derivation time interval, pickup ions are expected to be accelerated to several or even tens of times the original speed in the solar wind frame since the shock obliquity $\theta_{Bn} < 60^\circ$. Some of the particles are accelerated to high energies to form a double power-law spectrum. The pre-accelerated particles whose speed is beyond the injection threshold, which is usually around the de Hoffmann–Teller speed $V_{\rm dHT} = u_1 \sec\theta_{Bn}$, are able to be further accelerated by the highly oblique termination shock to higher energy. The acceleration process is similar to that in the case discussed in Section 6.3. So at the very high energies, the spectra resemble another double power-law spectrum. Eventually, the accelerated energy spectra should include two parts corresponding to two components of acceleration, respectively, with a transition and four power laws generated. Decker et al. (2006) found that the pitch angle anisotropy of the TSPs peaks at a high energy of $\sim$0.35 MeV. Since the anisotropy decreases with the increasing particle energy relative to the injection particle energy (E/E_0), the particles with an energy of $\sim$0.35 MeV

can be reasonably imaged as main injection particles for the second component acceleration. So, given the injection energy threshold as 0.35 MeV, the shock obliquity is estimated as $\theta_{Bn} \sim 87^{\circ}$. This is in agreement with the work of Florinski et al. (2008b), where the shock obliquity is estimated to vary between 80° and 88° along with time according to the first-order anisotropy distribution.

Zank et al. (1996) and Lee et al. (1996) pointed out that a strong cross-shock electric field may lead to multiple particle reflections or surfing on the shock surface to achieve a rapid energy gain. The shock surfing effect is more important for the acceleration of low energy particles, for which the pitch angle change rate due to the reflection by cross-shock electric field is comparatively larger. The FTE itself contains the term of the cross-shock electric field, so it is easy to incorporate the shock surfing acceleration mechanism for a global consideration in the anisotropic shock acceleration. Le Roux et al. (2007) compared the accelerated energy spectra under circumstances with or without the cross-shock electric field and found that the cross-shock electric field can change the low-energy part of spectra. Furthermore, for an oblique shock, the power-law spectra at the intermediate energies become harder if the cross-shock electric field is considered. These features are perhaps due to the fact that the reflecting by the cross-shock electric field makes the particles more anisotropic. Recently, we conducted a simulation to investigate the intensity change of the energy distribution function resulting from the shock surfing and found that the cross-shock electric field can essentially improve the acceleration efficiency, especially in a quasi-perpendicular shock. Although the initial work is performed, the role of the cross-shock electric field for termination shock acceleration and how and why it changes the shock acceleration spectra, acceleration efficiency, anisotropy, and spatial distribution of the energetic particle are not completely known. This will be our next consideration.

This work was supported in part by NASA under grants NNX08AP91G, NNX09AG29G, and NNX09AB24G and by NSF under MRI Grant 0923050. The authors acknowledge support from the National Natural Science Foundation of China (40890162, 41031066, 40921063, 40674084, 40904048), Research Fund for Recipient of Excellent Award of the Chinese Academy of Sciences President's Scholarship, and the Specialized Research Fund for State Key Laboratories. We thank Marcus Hohlmann and his High Energy Physics group at Florida Tech for making their high-performance grid computing cluster available for some of the computational analysis presented here.

REFERENCES

Ball, B., Zhang, M., Rassoul, H., & Linde, T. 2005, ApJ, 634, 1116
Chalov, S. V., & Fahr, H. J. 2000, A&A, 360, 281
Chalov, S. V., Fahr, H. J., & Izmodenov, V. 1997, A&A, 320, 659
Cummings, A. C., Stone, E. C., McDonald, F. B., et al. 2006, in AIP Conf. Proc. 858, Physics of the Inner Heliosheath: Voyager Observations, Theory, and Future Prospects, ed. J. Heerikhuisen (Melville, NY: AIP), 86
Decker, R. B. 1988, Space Sci. Rev., 48, 195
Decker, R. B., Krimigis, S. M., Roelof, E. C., et al. 2005, Science, 309, 2020
Decker, R. B., Roelof, E. C., Krimigis, S. M., & Hill, M. E. 2006, in AIP Conf. Proc. 858, Physics of the Inner Heliosheath: Voyager Observations, Theory, and Future Prospects, ed. J. Heerikhuisen (Melville, NY: AIP), 73
Drury, L. O'C. 1983, Rep. Prog. Phys., 46, 973
Florinski, V. 2009, Space Sci. Rev., 143, 111
Florinski, V., Decker, R. B., & le Roux, J. A. 2008a, J. Geophys. Res., 113, A07103
Florinski, V., Zank, G. P., & le Roux, J. A. 2008b, Adv. Space Res., 41, 361
Gardiner, C. W. 1983, Handbook of Stochastic Methods for Physics, Chemistry, and the Natural Sciences (Berlin: Springer)
Giacalone, J., & Kota, J. 2006, Space Sci. Rev., 124, 277
He, H. Q., & Qin, G. 2011, ApJ, 730, 46
Isenberg, P. A. 1997, J. Geophys. Res., 102, 4719
Jokipii, J. R. 1966, ApJ, 146, 480
Jokipii, J. R. 1982, ApJ, 255, 716
Klappong, K., Leerungnavarat, K., Chuychai, P., & Ruffolo, D. 2001, in Proc. 27th Int. Cosmic Ray Conf., Hamburg, 8, 3461
Kota, J. 1985, in Proc. 19th Int. Cosmic Ray Conf., 275
Kota, J., Manchester, W. B., Jokipii, J. R., de Zeeuw, D. L., & Gombosi, T. I. 2005, in AIP Conf. Proc., Vol. 781, The Physics of Collisionless Shocks, (Melville, NY: AIP), 201
Krülls, W. M., & Achterberg, A. 1994, A&A, 286, 314
Lee, M. A., Shapiro, V. D., & Sagdeev, R. Z. 1996, J. Geophys. Res., 101, 4777
le Roux, J. A., & Webb, G. M. 2009, ApJ, 693, 534
le Roux, J. A., Webb, G. M., Florinski, V., & Zank, G. P. 2007, ApJ, 662, 350
Luo, X., Zhang, M., Rassoul, H. K., & Pogorelov, N. V. 2011, ApJ, 730, 13
Northrop, T. G. 1963, The Adiabatic Motion of Charged Particles (New York: Interscience)
Parker, E. N. 1965, Planet. Space Sci., 13, 9
Qin, G., Zhang, M., Dwyer, J. R., Rassoul, H. K., & Mason, G. M. 2005, ApJ, 627, 562
Rossi, B. B., & Olbert, S. 1970, Introduction to the Physics of Space (New York: McGraw-Hill)
Schlickeiser, R. 2002, Cosmic Ray Astrophysics (Berlin: Springer)
Skilling, J. 1975, MNRAS, 172, 557
Stone, E. C., Cummings, A. C., McDonald, F. B., et al. 2005, Science, 309, 2017
Webb, G. M. 1985, ApJ, 296, 319
Webb, G. M., Axford, W. I., & Terasawa, T. 1983, ApJ, 270, 537
Webb, G. M., Martinic, N. J., & Moraal, H. 1982, in Proc. 17th Int. Cosmic Ray Conf., 10, 109
Zank, G. P., Pauls, H. L., Cairns, I. H., & Webb, G. M. 1996, J. Geophys. Res., 101, 457
Zhang, M. 1999, ApJ, 513, 409
Zhang, M. 2000, ApJ, 541, 428
Zhang, M. 2006, J. Geophys. Res., 111, A04208
Zhang, M., Qin, G., & Rassoul, H. 2009, ApJ, 692, 109